

Single Atomic Iron Site Catalysts *via* Benign Aqueous Synthesis for Durability Improvement in Proton-Exchange Membrane Fuels Cells

Mengjie Chen,^a David A. Cullen,^b Stavros Karakalos,^c Xiner Lu^d, Jiang Cui,^d A. Jeremy Kropf,^e Hemma Mistry,^e Kai He,^{d,z} Deborah J. Myers,^{e, *,z}, and Gang Wu^{a,*,z}

^aDepartment of Chemical and Biological Engineering, University at Buffalo, The State University of New York, Buffalo, NY 14260, USA

^bCenter for Nanophase Materials Sciences, Oak Ridge National Laboratory, Oak Ridge, TN 37831, USA

^c Department of Chemical Engineering, University of South Carolina, Columbia, SC 29208, USA

^d Department of Materials Science and Engineering, Clemson University, Clemson, SC 29634, USA

^e Chemical Sciences and Engineering Division, Argonne National Laboratory, Lemont, IL 60439, USA

*Electrochemical Society Member.

^z Corresponding authors:

kaihe@clemson.edu (K. He); dmyers@anl.gov (D. J. Myers); gangwu@buffalo.edu (G. Wu.)

Abstract:

Atomically-dispersed iron-nitrogen-carbon (Fe-N-C) catalysts have arisen as promising candidates for replacing the costly precious metal catalysts in fuel cells but still face some grand challenges, such as insufficient site density and durability. Herein, we report a self-assembly method in an aqueous solution to develop an atomically-dispersed iron catalyst with high oxygen reduction reaction (ORR) activity and activity stability in acidic electrolytes. As determined by high-resolution transmission electron microscopy (HR-TEM), X-ray absorption spectroscopy (XAS), and high-angle annular dark-field scanning transmission electron microscopy (HAADF-STEM), this benign aqueous synthesis strategy facilitates the formation of homogeneous atomic nitrogen-coordinated iron sites embedded in a popcorn-like porous graphitic carbon matrix. These catalyst properties contribute to the improved ORR kinetic current density and mass transport. By controlling synthesis chemistry, the correlation between structure and property is systematically investigated. The iron content is the most critical material property and can regulate site density and graphitic carbon structures in the catalyst, impacting catalytic activity and stability. The enhanced performance and durability were examined in both acidic aqueous electrolytes and membrane electrode assemblies.

Keywords: Atomic iron catalysts; self-assembly; oxygen reduction reaction; PGM-free PEMFC catalyst; aqueous synthesis; fuel cells

Introduction

Platinum-group-metal (PGM)-free cathode catalysts have been investigated extensively in the last decade.¹⁻⁴ Among other types of PGM-free catalysts, Fe-based catalysts demonstrate the most promising performance in acidic electrolyte, including proton exchange membrane fuel cells (PEMFCs) due to their high activity toward the oxygen reduction reaction (ORR) and high selectivity *via* the four-electron pathway.⁵⁻⁷ The significant challenges to further develop Fe-based catalysts for practical application, such as PEMFCs, include: (i) enhancing ORR mass activity to reduce PEMFC cathode catalyst layer thickness, (ii) tuning catalyst microstructure and morphology for improved active site utilization and mass transport, and (iii) overcoming rapid performance degradation issues. There are two primary pathways to improve catalyst activity. One pathway is to increase the density of active sites by engineering the catalyst nanostructure, shape, and by modifying the catalyst support. The other is to enhance the intrinsic activity of the active sites by modifying local coordination and carbon structures.⁸⁻¹⁰ Generally, these two strategies do not interfere with each other and can be explored simultaneously. Recently, a consensus has emerged that the active metal site precursor can be confined into a nanoscale space to prepare single-metal site catalysts, maximizing the utilization of active sites and significantly enhancing the performance.¹¹⁻¹⁴ Microscopy, spectroscopy, and theoretical calculations indicate that N-coordinated Fe moieties are the most likely active ORR sites.^{15, 16} Extensive studies are focused on increasing the number of atomically-dispersed FeN_x active sites in carbon-based catalysts.¹⁷⁻²⁰ However, the ORR activity of current catalysts is still limited due to the insufficient density of active sites and their low utilization.⁷ When the transition metal amount is further increased during synthesis, metal clusters are formed during the critical thermal activation process.^{21, 22} The density of active sites cannot be further increased due to the limitation of available nitrogen sites in the

carbon matrix to stabilize the Fe sites. Improving the intrinsic activity of FeN_x via tuning the chemical environment and coordination structure is also essential to reduce ORR overpotential, optimize the adsorption energy of intermediates, and enhance charge transfer.²³⁻²⁵

Among precursors studied for single Fe site catalysts, ZIF-8s can facilitate the formation of single-metal sites by anchoring and isolating targeted metal ions effectively due to the abundant zinc and nitrogen sites and the dominant micropores. During thermal activation, the targeted metal ions are inhibited from migrating and aggregating and can easily bond with surrounding N ligands. Currently, most reported single Fe site catalysts derived from ZIF-8 precursors are prepared from harmful and high-cost organic solvents such as methanol and dimethylformamide.^{26, 27} Even though some studies report innovative methods for ZIF-8 synthesis in the solid phase,²⁸ those materials still suffer from a complicated process and heterogeneous morphology.^{29, 30} Compared with synthesis in organic solvents and in the solid phase, the synthesis of ZIF-8s in aqueous solution has particular advantages for catalyst synthesis in terms of ORR activity, performance in PEMFCs, economics, and the environment.³¹ Also, aqueous synthesis may provide a new opportunity to strengthen the local Fe-N coordination and yield a highly graphitic carbon structure, which is critical for stable Fe-N-C catalysts with enhanced tolerance to demetallation and carbon corrosion during the ORR.³²

Herein, we demonstrated a self-assembly method to prepare a highly active and durable atomically-dispersed Fe-N-C catalyst *via* a benign aqueous synthesis procedure. The resulting catalyst presents homogeneous FeN_4 active sites in a popcorn-like graphitic carbon matrix, which was characterized by X-ray absorption spectroscopy (XAS) and low-voltage scanning transmission electron microscopy (STEM) with electron energy loss spectroscopy (EELS). Moreover, the method allows the use of a high Fe content which catalyzes the formation of

graphitic carbon which has enhanced resistance to corrosion resulting in improved durability in the PEMFC environment.

Experimental details

Catalyst synthesis. Iron nitrate nonahydrate and zinc nitrate hexahydrate (0.49 mol l⁻¹) were dissolved in an aqueous solution followed by sonication for 10 min. Typically, the molar ratio of Fe and Zn ions was adjustable with ratios of $x:1$, where x is the atomic percent ratio of Fe to Zn in precursor during synthesis. After mixing with 2-methylimidazole solution and stirring for 12 hours at room temperature, the Fe-doped ZIF-8 precursor was collected using centrifugation, followed by thorough washing of the precipitate with ethanol at least five times. The precipitate was dried at 60 °C in a vacuum oven for 12 hours. The Fe-doped ZIF-8 precursor was carbonized at 1100°C in a tube furnace under Ar flow for one hour to obtain the catalyst. The Fe-doped ZIF-8 precursor was labeled as Fe-ZIF- x , and the catalyst as Fe-N-C- x . The Fe-free nitrogen-doped carbon (NC) was also prepared from the ZIF-8 precursor through identical procedures, but omitting Fe ions.

Physical characterization. The catalyst was studied using scanning electron microscopy (SEM) on a Hitachi SU 70 microscope. X-ray diffraction (XRD) characterization was performed on a Rigaku Ultima IV diffractometer with Cu K α X-rays to present crystal phases in each sample. The N₂ isothermal adsorption/desorption was recorded at 77K on a Micromeritics TriStar II. Samples were degassed at 150 °C for five hours under vacuum before nitrogen physisorption measurements. Raman spectroscopy was performed using a Renishaw Raman system at 514 nm excitation. Samples were prepared as ink on a standard microscope glass slide, with the excitation laser focused through a 50 \times microscope objective for a total interrogation spot size of 1.0-micron diameter. X-ray photoelectron spectroscopy (XPS) was performed using a Kratos AXIS Ultra DLD

XPS system equipped with a hemispherical energy analyzer and a monochromatic Al K α source. The monochromatic Al K α source was operated at 15 keV and 150 W; the pass energy was fixed at 40 eV for the high-resolution scans. All samples were prepared as pressed powders supported on a metal bar for the XPS measurements. Atomic-resolution micrographs were obtained using a Nion Ultra STEM U100 microscope operated at 60 keV and equipped with a Gatan Enfina electron energy loss spectrometer (EELS). EELS spectra, used to evaluate the composition of the atomically-dispersed Fe sites, were processed using the open-source Hyperspy python library to remove noise. The high-resolution transmission electron microscopy (HR-TEM) and energy-dispersive X-ray spectroscopy (EDS) elemental mapping analysis experiments were performed on a Hitachi H9500 TEM and a SU9000 STEM. X-ray absorption spectroscopy (XAS) experiments were carried out in fluorescence geometry at beamline 10BM, Materials Research Collaborative Access Team (MRCAT), Advanced Photon Source (APS), Argonne National Laboratory (ANL). Data reduction, data analysis, and fitting of the extended region of the spectra were performed with the Athena, Artemis, and IFEFFIT software packages.³³

Electrochemical and fuel cell measurements. All electrochemical measurements were conducted using a CHI electrochemical workstation (CHI760b) coupled with a rotating-ring disk electrode (RRDE, Pine, AFMSRCE 3005) in a three-electrode system. A graphite rod and a Hg/Hg₂SO₄ (K₂SO₄-sat.) electrode were used as the counter and reference electrodes, respectively. The working electrode of the RRDE was a glassy carbon electrode covered by a thin film of the catalysts dispersed in Nafion® ionomer. Each catalyst powder (5 mg) was ultrasonically dispersed in a 0.5 mL mixture of isopropanol and Nafion® (5 wt.%) solution to prepare the ink. The ink was then drop-cast on the glassy carbon working electrode of the RRDE to achieve a mass loading of 0.6 mg catalyst/cm². The catalyst-coated working electrode was subjected to cyclic voltammetry

(CV) in O₂-saturated 0.5 M H₂SO₄ to activate the catalysts. The electrocatalytic ORR activity for PGM-free catalysts was tested by steady-state measurement using staircase voltammetry with a step of 0.05 V at 30 s from 1.0 to 0.05 V *vs.* RHE in O₂-saturated 0.5 M H₂SO₄ at 25 °C and a rotation rate of 900 rpm. As a reference, a Pt/C catalyst was tested using staircase voltammetry in O₂-saturated 0.1 M HClO₄ with a loading of 60 $\mu\text{g}_{\text{Pt}}/\text{cm}^2$. Catalyst stability was studied by potential cycling from 0.6 to 1.0 V in 0.5 M H₂SO₄ electrolyte at 25°C and holding the potential at 0.8 V for 20 hours. The Fe-N-C catalysts were used to prepare cathodes for membrane-electrode assembly (MEA) tests. The cathode catalyst inks were dispersed by ultrasonication of the catalyst in 2-proposal, de-ionized water, and Nafion® suspension for three hours under an ice bath. The inks were blade-painted on one side of commercial gas diffusion layers (GDLs) until the cathode catalyst loading reached \sim 4.0 mg cm⁻². A Pt/C anode with a loading of 0.2 mg_{Pt} cm⁻² was used and Nafion® 211 (N211) was used as a membrane. Both cathode and anode were transferred onto the N211 membrane by hot-pressing. The single-cell performance was evaluated using a fuel cell test station (100 W, Scribner 850e, Scribner Associates). For the polarization curve test, air/oxygen flowing at 1000 sccm and H₂ flowing at 300 sccm were used as the cathode and anode reactants, respectively. The cell voltage was held at 0.7 V for the constant voltage test and the flow rates were held at 200/200 sccm. The absolute pressure of reactant gas applied to the MEAs was 1.0 bar, (*i.e.*, 0.5 bar gauge pressure). The active area of both the anode and cathode of the MEA was 5.0 cm².

Results and discussion

Catalyst design, synthesis, and morphology.

A self-assembly aqueous synthesis method for atomically-dispersed Fe-N-C catalysts was developed in this study, as shown in **Figure 1a**. During the synthesis of the Fe-doped ZIF-8 precursor in water, the coordination bond between organic linkers and zinc nodes will be broken

by H₂O molecules, exposing the unsaturated N sites for coordinating with Fe ions.³⁴ Meanwhile, the fast crystallization process of ZIF-8 in an aqueous solvent can lead to the formation of abundant point defects, *e.g.*, missing node defects, which can expose more linker sites.³⁵ Thus, iron ions can be anchored by those unsaturated nitrogen sites in the precursors. After the self-assembly process, the ZIF-8 crystal structure is not significantly changed by the doped Fe ions (**Figure 1b**). Afterward, the Fe-ZIF precursors are subjected to thermal conversion under Ar atmosphere to form the Fe-N-C catalyst. The abundant nitrogen sites from the linkers provide anchoring sites to stabilize the single Fe ions and generate N-coordinated Fe sites. After the pyrolysis, the appearance of typical carbon peaks and the absence of ZIF-8 peaks confirm the complete carbonization of the precursor (**Figure 1b**). Crystalline Fe species are not detected in the XRD patterns. The Fe-ZIF precursor exhibits a polyhedron morphology with blurred edges and vertices (**Figure 1c**). The resulting catalyst morphology becomes irregular, showing popcorn-like wrinkled surfaces (**Figure 1d**). The defect-rich and distorted Fe-ZIF precursor structure, attributed to the unsaturated N sites, was observed by HR-TEM (**Figure 1e**). HR-TEM confirms the porous structure (**Figure 1f**) and graphitic carbon layers (**Figure 1g**) in the catalyst after the pyrolysis. Further STEM-EDS elemental mappings (**Figure 1h-k**) verified the uniformly dispersed Fe sites. Moreover, signals for Fe, N, and C are overlapped each other. A series of Fe-N-C catalysts were prepared in a similar manner to that of the catalyst shown in Fig. 1 for a comparative study of the effect of Fe content. The corresponding catalysts are denoted as Fe-N-C-*x* (where *x* is the atomic percent ratio of Fe to Zn in the precursor during synthesis).

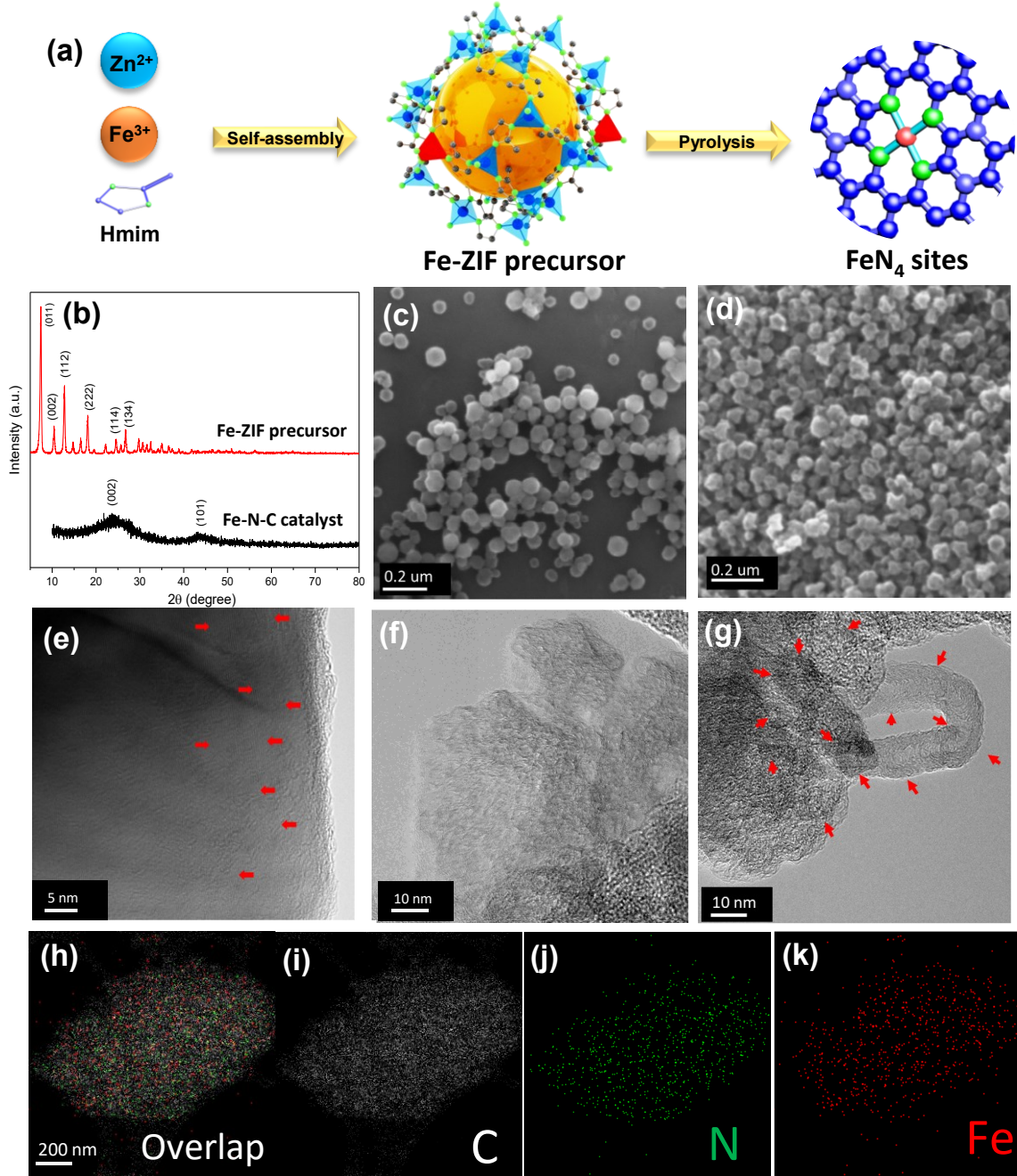


Figure 1. (a) Self-assembly synthetic scheme of Fe-N-C catalysts. (b) X-ray diffraction patterns of Fe-ZIF precursor and Fe-N-C catalyst. SEM images of (c) Fe-ZIF precursors and (d) Fe-N-C catalyst. HR-TEM images of (e) Fe-ZIF precursors and (f, g) Fe-N-C catalysts (the red arrows point to the defects or graphitic carbon layers). (h-k) STEM-EDS elemental mapping of C, N, and Fe for Fe-N-C catalysts.

Atomically iron sites dispersed on a popcorn-like carbon matrix.

In the low-voltage STEM images (**Figure 2a**), the Fe-N-C-2.5 catalyst shows a popcorn-like nanostructure. This irregular popcorn-like structure can increase mass transport and improve active site utilization.^{36, 37} HR-STEM provides direct evidence that atomically-dispersed Fe sites are embedded into the carbon matrix and distributed homogeneously in the Fe-N-C catalyst (**Figure 2b**). The homogeneously-dispersed Fe sites are coordinated with nitrogen and distributed among the graphitic carbon layers, further confirmed by EELS (**Figure 2c** and **2d**). Such homogeneous atomically-dispersed nitrogen-coordinated iron sites are considered the active sites for the ORR.

Furthermore, graphitic carbon layers are observed in the STEM images. A graphitic carbon is known to be beneficial for catalyst stability.³⁸ The Fe-N-C-10 catalyst was also examined using STEM. This catalyst exhibits similar popcorn-like carbon morphology (**Figure 2e**) as that observed for the Fe-N-C-2.5 catalyst. According to the STEM and EELS results (**Figure 2f-h**), the Fe-N-C-10 catalyst also shows good dispersion of nitrogen-coordinated iron sites on the graphitic carbon matrix; Fe aggregates were not observed. STEM is a local characterization technique. XAS is a complementary characterization technique to STEM imaging as it provides a more global and bulk characterization of Fe speciation of the catalysts. XAS data were acquired for the Fe-N-C catalysts and Fe-ZIF precursor to identifying the coordination environment of Fe.

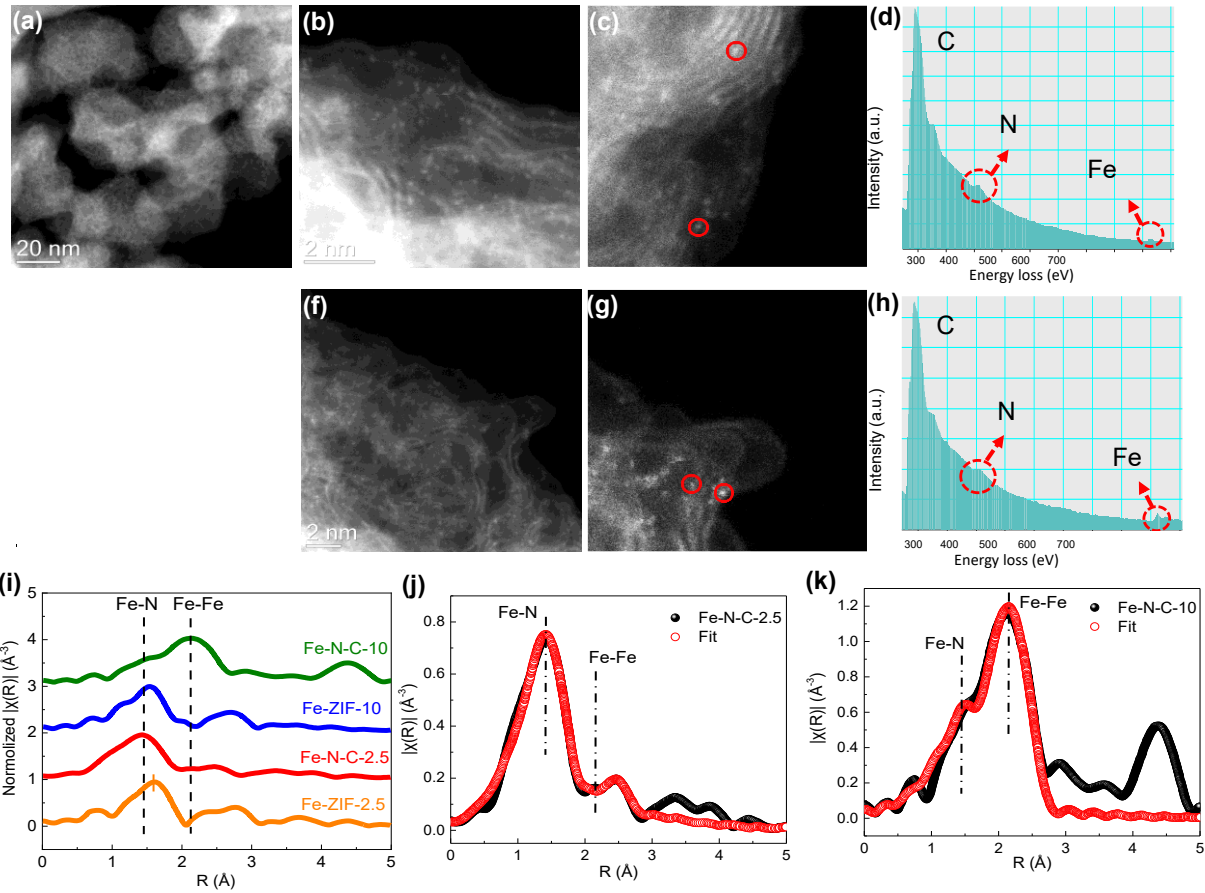


Figure 2. HAADF-STEM image of the overall morphology of Fe-N-C-2.5 catalyst (a). HAADF-STEM image of atomically dispersed iron sites (bright dots) throughout the carbon matrix in the Fe-N-C-2.5 catalyst (b). The Fe-N-C-2.5 catalyst and corresponding EELS point spectra from the atomic sites circled in red (c and d). HAADF-STEM image of the overall morphology of Fe-N-C-10 catalysts (e). HAADF-STEM image of atomically dispersed iron sites (bright dots) throughout the carbon matrix in the Fe-N-C-10 catalyst (f). Fe-N-C-10 catalyst and corresponding EELS spectra from the atomic sites circled in red (g and h). Fourier transforms of the Fe K-edge EXAFS spectra and corresponding fit results (i-k).

The Fourier transforms of the Fe K-edge extended X-ray absorption fine structure (EXAFS) shows that Fe in both Fe-ZIF precursors is coordinated only to a light element with a short bond distance, lacking the Fe-Fe second shell scattering at 2.7 and 4.6 Å (scattering path lengths shown in the Fourier transforms are not phase corrected), which would be observed for Fe oxides. Moreover, a Fe-Fe first shell scattering path at ~2.2 Å is not evident in the Fourier transforms for both Fe-ZIF precursors, suggesting that most iron ions are coordinated with nitrogen atoms in the ZIF crystals and not in the form of metallic Fe clusters (**Figure 2i**)^{39, 40}. These data indicate that the nitrogen sites in the ZIF-8 lattice can effectively anchor the iron ions from the self-assembly in the aqueous solution. The anchored Fe ions show lower mobility and uniform distribution throughout the precursor due to spatial confinement⁴¹. Compared with the Fe-ZIF-2.5 precursor, the Fe-N bond length is shorter in the Fe-N-C-2.5 catalyst, as expected with conversion of the tetrahedral coordination environment to a square planar, square pyramidal, or octahedral coordination environment. There are again no evident Fe-Fe first or second shell scattering paths in the Fourier transform for this catalyst. This indicates that the catalyst is mostly free of iron clusters and oxides, supporting the STEM data showing only atomically-dispersed Fe centers. The EXAFS data fit results (**Table 1**) support the observation that this catalyst is substantially free of iron particles. A minor Fe-Fe scattering path was included in the fit, resulting in an Fe-Fe coordination number of 1.0. When normalized to the total of all Fe scattering paths include in the fit and taking into account the expected Fe-Fe coordination number of 8 for bulk metallic Fe, the percentage of Fe that is in an Fe metal-like coordination is <13%. However, a substantial first shell Fe-Fe scattering path is evident in the Fourier transform of the EXAFS data for the Fe-N-C-10 catalysts (**Fig. 2k**) at ~2.2 Å and a second shell scattering path is even evident at ~4.5 Å, indicative of the presence of large clusters or particles of Fe. Two Fe-Fe scattering paths with substantial

coordination numbers were used to fit the EXAFS data (**Table 1**). An estimate of the percentage of total Fe with Fe metal-like coordination, based on the coordination number of 3.7, is 46%. These results indicate that the spatial confinement afforded by zinc is limited. When iron content is high in the precursor, the additional iron tends to form iron clusters during heat treatment regardless of the initial coordination of Fe with unsaturated N sites during the thermal conversion.

Table 1. Summary of EXAFS fitting results for the Fe-N-C catalysts.

Catalyst	Scattering Path	Coordination Number	Path Length (Å)	$\sigma^2 \times 10^3$ (Å ²)	E ₀ (eV)
Fe-N-C-2.5*	Fe-N/O	5.6±0.7	1.932±0.011	14	-6
	Fe-Fe	1.0±1.0	2.908±0.033	20	
Fe-N-C-10**	Fe-N/O	4.9±3.7	1.930±0.031	20	-6
	Fe-Fe	3.7±1.7	2.487±0.011	6	
	Fe-Fe	1.5±0.8	2.887±0.036	6	

Fitting parameters:

S_0^2 was fixed at 0.71 as obtained by fitting the reference foil.

E₀ fixed

*k-weight = 2, R-factor: 0.002, k range: 3.0 – 10.5, R range: 1.0 – 2.9

**Constrained $\sigma^2_{\text{Fe-Fe}} = \sigma^2_{\text{Fe-Fe}}$, k-weight = 2, R-factor = 0.008, k range: 3 – 12, R range: 1.0 – 2.7

Structure comparison of Fe-N-C catalysts.

To reveal the correlation between Fe content and structure of Fe-N-C catalysts, further characterization was performed on the Fe-N-C-2.5 and Fe-N-C-10 catalysts. As shown in **Figure 3a**, the XRD patterns of both are dominated by two peaks, showing the characteristics of a carbon crystal plane with C (002) at ca. 24° and C (101) at ca. 43°. No prominent crystalline iron species were detected for the Fe-N-C-10 catalyst. Compared with carbon structure patterns of the Fe-N-

C-2.5 catalyst, the Fe-N-C-10 catalyst exhibits a positive shift of peak position, which is closer to the peak positions expected for those of hexagonal graphite, indicating the degree of graphitization is significantly enhanced.^{42, 43} Moreover, the sharpness of the C (101) crystal plane peak for the Fe-N-C-10 catalyst further reveals that there are a large number of well-aligned graphitic planes and domains. This result is in good agreement with Raman spectra (**Figure 3b**). Two significant Raman peaks at ca. 1350 cm⁻¹ and 1590 cm⁻¹ were observed for the Fe-N-C catalysts, ascribed to D and G bands, respectively.⁴⁴ The D band corresponds to disordered or defective carbon structures from six-sided hexagonal rings.⁴⁵ In contrast, the G band can result from sp² hybridized C-C bonds in a two-dimensional hexagonal lattice.^{46, 47} Compared with the Fe-N-C-2.5 catalyst, the lower ratio of D to G peak areas (A_D/A_G) for the Fe-N-C-10 catalyst indicates that the graphitic carbon phase is more prevalent in this catalyst. The narrower D band of the Fe-N-C-10 catalyst further suggests an overall enhancement of graphitization. Moreover, the 2D peak noted as the second-order of the D peak appeared and became even sharper in the case of Fe-N-C-10, indicative of graphitic features.

The C1s XPS results (**Figure 3c**) show that the intensity of the C=C peaks is higher and the peaks narrower for the Fe-N-C-10 catalyst versus those observed for the Fe-N-C-2.5 catalyst, in good agreement with the Raman results showing a higher degree of graphitization. The N 1s peak can be fit with four peaks, which can be assigned to pyridinic-N, Fe-N species, graphitic-N, and oxidized-N, respectively (**Figure 3d**). The pyridinic nitrogen can act as anchor sites to coordinate with Fe sites and the graphitic nitrogen can modify the electronic structure of carbon materials.⁴⁸ It should be noted that the Fe-N-C-10 catalyst demonstrates a dominant graphitic nitrogen peak with a minor component of pyridinic nitrogen, which is consistent with the Raman data showing

lower a lower defect density. **Table 2** summarizes the elemental composition for the Fe-N-C-2.5 and Fe-N-C-10 catalysts determined by XPS.

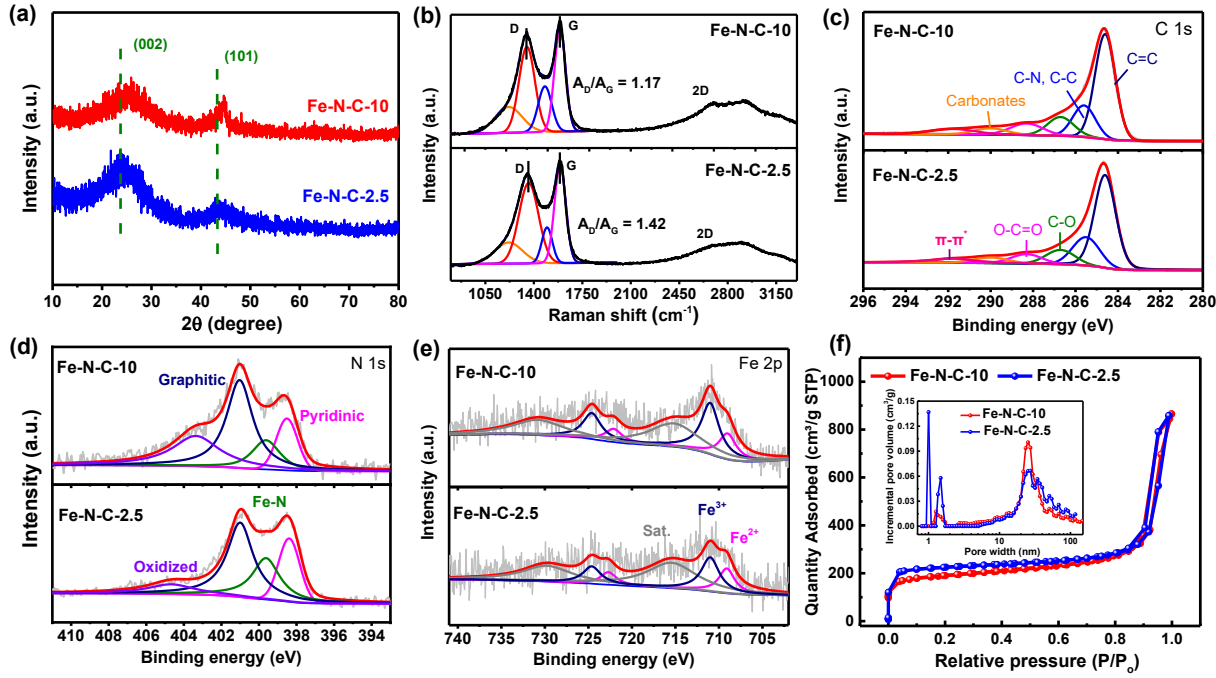


Figure 3. (a) X-ray diffraction patterns, (b) Raman spectra, and X-ray photoelectron spectroscopy of C 1s (c), N 1s (d), and Fe 2p (e) for Fe-N-C-10 and Fe-N-C-2.5 catalysts. (f) N_2 isotherm plots and pore size distribution (inset) of Fe-N-C-10 and Fe-N-C-2.5 catalysts.

Table 2. Elemental quantification determined by XPS.

Samples	Fe (wt%)	N (wt%)	O (wt%)	Zn (wt%)	C (wt%)
Fe-N-C-2.5	1.6	6.9	6.3	2.7	82.5
Fe-N-C-10	3.4	4.1	5.4	0.8	87.3

All the characterization results clearly verify a higher degree of graphitization for the Fe-N-C-10 catalyst. This could be attributed to the formation of iron clusters, due to the higher Fe content,

which can catalyze the formation of graphitic carbon. The Fe 2p XPS spectra indicate that the iron species in the surface environment of catalyst have a valence between 2+ and 3+ (**Figure 3e**), which is in good agreement with the results from XAS showing an edge energy that is intermediate between that typically observed for Fe ²⁺ and Fe ³⁺ species. The specific surface area and pore size distribution of the Fe-N-C catalysts were also determined (**Figure 3f**). The Fe-N-C-2.5 catalyst shows a higher surface area ($738 \text{ m}^2 \text{ g}^{-1}$) and dominant micropore volume, evidenced by an increase in the N_2 uptake at low pressure. The decreased surface area ($636 \text{ m}^2 \text{ g}^{-1}$) of the Fe-N-C-10 catalyst can be attributed to lower microporous volume and can most likely be attributed to the catalyzation of the formation of graphitic carbon by metallic Fe clusters. Moreover, both catalysts exhibit a high volume of mesopores and macropores, generated through void space due to the popcorn-like morphology. This feature can enhance the mass transport and ionomer distribution in the cathode catalyst layer of the PEMFC.

Electrocatalytic ORR activity and stability.

Figure 4 shows the electrochemical measurements in O_2 -saturated 0.5 M H_2SO_4 for NC and Fe-N-C catalysts with varying Fe content. The ORR activity was observed to be dependent on the Fe content of the catalyst precursor (**Figure 4a**). Without any Fe addition, the nitrogen-doped carbon (NC) catalyst exhibits insufficient ORR activity with a half-wave potential ($E_{1/2}$) of 0.58 V. Addition of 0.5 at% Fe to the precursor leads to a considerable improvement in ORR activity, evidenced by the more positive $E_{1/2}$ of 0.77 V, revealing the formation of ORR active sites with the addition of Fe. Among various precursor Fe contents studied, from 0.5 to 30 at.%, the catalyst formed from a precursor with 2.5 at.% Fe was found to have the highest ORR activity. The Fe-N-C-2.5 catalyst achieved an onset potential (E_{onset}) of 0.97 V and an $E_{1/2}$ of 0.86 V *vs.* RHE, only 10

mV lower than that of a commercial Pt/C catalyst ($60\mu\text{g}_{\text{Pt}}/\text{cm}^2$, $E_{1/2} = 0.87$ V in 0.1 M HClO_4 solution). The Fe-N-C-10 catalysts exhibited reduced ORR activity (**Table 2**) compared to that of the Fe-N-C-2.5 catalyst, exhibiting moderate activity with an $E_{1/2}$ of 0.83 V. This suggests that the gravimetric density of active sites is lower in the Fe-N-C-10 catalyst, indicating that the effective Fe available for or remaining in FeN_x active sites is reduced with the addition of more Fe to the precursor. This indicates that a fraction of the iron ions coordinated to N sites in the precursor can no longer be stabilized by the N sites and are subject to agglomeration during the thermal conversion. The formation of iron clusters/nanoparticles does not benefit the ORR activity, causing a decreased active site density and also decreasing porosity and surface area.²² When the iron doping content is further increased to 30 at.%, a dramatic loss of ORR catalyst activity is observed, indicating further reduction of the gravimetric density of FeN_x active sites due to the formation of iron clusters or nanoparticles. Comparing the ORR peroxide yield (**Figure 4b**), the nitrogen-doped carbon shows very low 4e^- selectivity, generating high yields of peroxide. In contrast, all the Fe-N-C catalysts show predominantly a 4e^- reduction pathway with peroxide yields lower than 5%.

The stability of catalysts is generally related to the structure of the carbon. Two different catalysts (*i.e.*, Fe-N-C-10 and Fe-N-C-2.5) were studied using two different protocols, including potential cycling from 0.6 to 0.95 V (**Figure 4c** and **4d**) and holding at a constant potential of 0.8 V for 20 h (**Figure 4e** and **4f**). After 5,000 potential cycles in O_2 -saturated 0.5 M H_2SO_4 , the Fe-N-C-2.5 catalyst demonstrates moderate degradation with 36 mV loss in $E_{1/2}$ and no noticeable change in E_{onset} . The Fe-N-C-10 catalyst exhibited improved catalyst durability with only 11 mV loss in $E_{1/2}$. In addition, a constant potential test was performed by holding the catalysts at a high potential of 0.8 V in O_2 -saturated 0.5 M H_2SO_4 . The Fe-N-C-2.5 catalyst exhibited moderate degradation as a result of the 20 h 0.8 V potential hold test, with a 33 mV loss of $E_{1/2}$ and the Fe-

N-C-10 catalyst demonstrated improved stability with only 19 mV loss of $E_{1/2}$. Given that the broken Fe-N coordination and carbon oxidation mainly contribute to the catalyst degradation,⁴⁹⁻⁵¹ improved durability of the Fe-N-C-10 catalysts can be attributed to the robust carbon with a higher degree of graphitization, which has been confirmed by using a variety of characterization techniques.

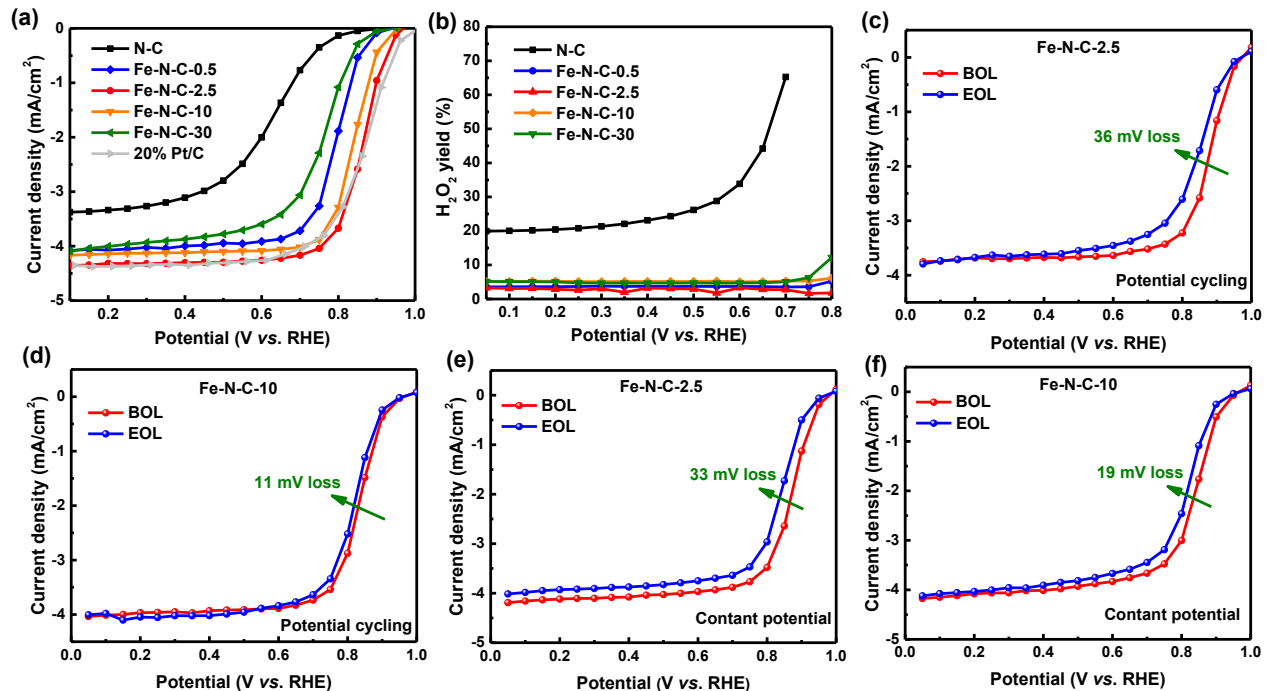


Figure 4. ORR polarization curves of NC, Fe-N-C catalyst in O₂-saturated 0.5 M H₂SO₄, and Pt/C catalyst in 0.1 M HClO₄ (a). H₂O₂ yield of Fe-N-C catalysts as a function of Fe content (b). Accelerated stress tests by potential cycling from 0.6-1.0 V for 5,000 cycles under O₂ for Fe-N-C-2.5 catalyst (c) and Fe-N-C-10 catalyst (d). Stability test by holding potential at 0.8 V under O₂ for 20 h of Fe-N-C-2.5 catalyst (e) and Fe-N-C-10 catalyst (f).

Fuel cell performance of Fe-N-C catalysts.

The Fe-N-C-2.5 and Fe-N-C-10 catalysts were further studied in MEAs under both O₂ and air cathode environments. Firstly, to identify the mass activity and minimize the mass transport losses,

the MEA is studied under H₂-O₂ conditions (**Figure 6a**). The measured open-cell voltage (OCV) for the Fe-N-C-2.5 catalyst was approximately 0.97 V, consistent with RDE tests in acidic media. The current density at 0.90 V_{iR-free} is 24 mA cm⁻², indicating a high ORR activity for a PGM-free catalyst.⁵² The Fe-N-C-10 catalyst shows a lower activity, only generating a current density of 8 mA cm⁻² at 0.90 V_{iR-free}.

In addition to ORR mass activity, which is the predominant property determining the high voltage current density, peak power density is also affected by ionic conductivity, electrical conductivity, and mass transport in the cathode catalyst layer. The MEA performance was further evaluated under realistic H₂-air conditions (**Figure 6a**). Both catalysts demonstrated good performance, generating current densities of 350 and 240 mA/cm² at 0.675 V, respectively. The maximum power density of 0.355 W cm⁻² is achieved for the Fe-N-C-2.5 catalyst. The MEA with the Fe-N-C-10 catalyst yielded a maximum power density of 0.33 W cm⁻². These Fe-N-C catalysts synthesized from an aqueous solution contain a unique popcorn-like nanostructure and a large quantity of mesopore/macropores. Such morphologies could expose increased FeN_x active sites at three-phase interfaces within the cathode. The substantial meso/macropores in these catalysts are beneficial for mass transport and increasing power density. However, there is still a noticeable performance difference between O₂ and air, indicating that mass transport in the thick cathode is still a primary limitation, especially when compared to the mass transport losses in Pt/C cathodes that are approximately and order of magnitude thinner (at 0.1 mgPt/cm² loading). Current Fe-N-C cathodes generate lower performance than Pt-based ones, primarily due to their lower active site density and the lower intrinsic activity of these sites.⁷ Therefore, a higher catalyst loading is often necessary for generating considerable current densities. Such a thick Fe-N-C cathode catalyst layer also leads to increased resistance to the transport of O₂ and protons. In addition, water management

in the thick Fe-N-C cathode becomes more challenging and the cathodes often suffer from serious water flooding issues, especially in the voltage region controlled by mass transport. The engineering of catalyst porosity, morphologies, and nanostructure can mitigate mass transport issues to enhance performance and to concomitantly enhance durability. For example, we recently developed a variety of approaches to create favorable hierarchical pore networks in catalysts by using templates, electrospinning, and surfactants.^{6, 48, 53, 54} In parallel, enhancing intrinsic activity and increasing site density effectively reduce the loading of catalyst needed, thus decreasing mass transport losses related to electrode thickness and increasing MEA performance.

The short-term durability of these Fe-N-C catalysts is also evaluated by holding the voltage at 0.7 V (**Figure 6b**) using air as the cathode gas. The voltage-current (VI) polarization plots are recorded during the durability test to monitor the degradation process. After an 18-hour test, 58% of the initial current density was retained for the MEA with the Fe-N-C-2.5 catalyst. The polarization curve demonstrates apparent degradation across the entire voltage range, indicating disappointing durability (**Figure 6c**). The rapid activity loss at the initial stage is likely due to Fe demetallation from the FeN_x active initiated by the corrosion/oxidation of the surrounding carbon. On the contrary, the Fe-N-C-10 catalyst shows little degradation after a 16-hour test at 0.7 V, indicating encouraging durability. The much-enhanced durability is possibly attributed to the high carbon oxidation resistance from the graphitic carbon structure observed in this catalyst, which can stabilize FeN_x sites and prevent them from iron demetallation. Carbon electrochemical oxidation to form oxygen-containing functional groups often occurs at high potentials and temperatures. These functional group can decrease the intrinsic activity of FeN_x active sites by changing the adsorption energy of O₂ and intermediates.⁵⁵ Moreover, such chemical/electrochemical oxidation of carbon next to FeN_x sites may destroy the active sites and

cause iron demetalation.⁵⁶ Since the Fe-N-C-10 catalyst contains highly-graphitized carbon structures, the enhanced durability may derive from the high carbon-oxidation resistance. Another factor is that the dominant micropore population of Fe-N-C-2.5 can accelerate the demetallation of active sites ascribed to a Le Chatelier-type shift in the $\text{FeN}_4/\text{Fe}^{2+}$ thermodynamic equilibrium.⁵⁷ A high microporosity typically leads to a faster initial ORR performance loss.⁵⁸ Therefore, the reduced micropore volume of the Fe-N-C-10 catalyst could be beneficial to stability by mitigating demetallation. Overall, Fe-N-C catalysts' performance and long-term durability are still grand challenges for practical application in fuel cells. Innovative catalyst design and MEA fabrication are needed to address current performance and durability issues.

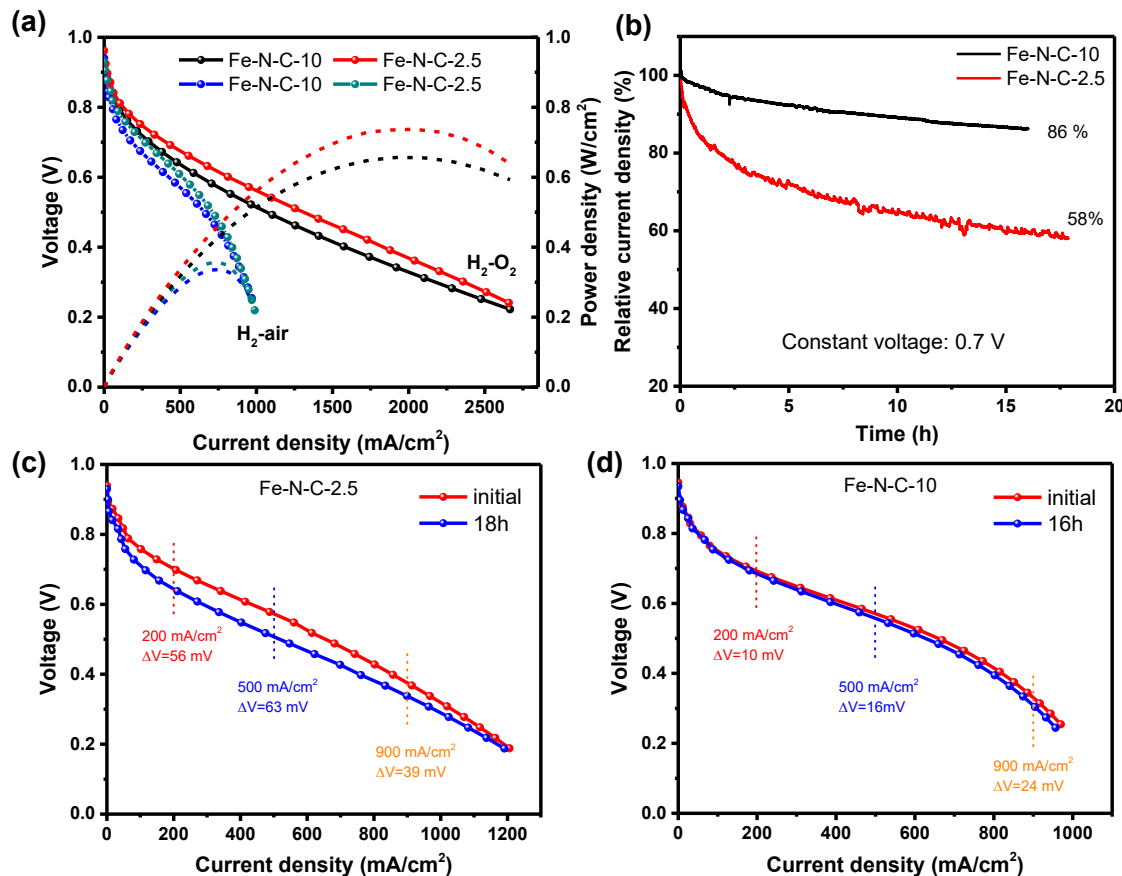


Figure 5. (a) Fuel cell performance of Fe-N-C catalysts under $\text{H}_2\text{-O}_2$ or $\text{H}_2\text{-air}$ conditions. (b) Fuel cell current retention during the voltage hold durability test. (c) Polarization curves of Fe-N-C-2.5 catalyst before and after voltage hold durability test. (d) Polarization curves of Fe-N-C-10 catalyst

before and after durability test. Test conditions: cathode loading of ~4.0 mg/cm², anode loading of 0.2 mg_{Pt}/cm², 80 °C, 100% relative humidity, 1.0 bar pressure.

Conclusions

In summary, unlike traditional organic solvents, this work reports an effective aqueous strategy to prepare atomically-dispersed single iron site Fe-N-C catalysts. By varying iron content in the precursor from 0 to 30 at.%, we were able to tune the ORR activity and durability of the catalyst. Using advanced characterization, including X-ray absorption spectroscopy and high-angle annular dark-field scanning transmission electron microscopy, the atomically dispersed FeN_x sites were confirmed in the best-performing Fe-N-C catalyst derived from a precursor with Fe content of 2.5 at%. Increased Fe content in the precursor failed to improve catalyst activity further, but rather decreased ORR activity. Extensive characterization was performed on the catalysts derived from precursors with 2.5 and 10% at.% Fe and comparisons of composition, structure, activity, performance, and durability were made for these two catalysts. The ORR activity and stability are closely correlated with the porosity and the graphitic carbon structure of catalysts, which controls the site density and carbon corrosion tolerance adjacent to active sites. While the Fe-N-C-10 catalyst exhibited slightly lower activity, it demonstrated significantly enhanced stability compared to the most active Fe-N-C-2.5 catalyst. It was proposed that this enhanced stability originated from the graphitic carbon structure and less dominant microporosity observed for the Fe-N-C-10 catalyst. Further performance and durability improvements of Fe-N-C catalysts should focus on increasing FeN_x site density by engineering catalyst morphology and enhancing intrinsic activity and stability of FeN_x sites by modifying the nature of Fe-N coordination and local carbon structures. These studies show that an optimal trade-off of activity and stability is critical in the design of efficient Fe-N-C catalysts.⁵⁹

Acknowledgement

The authors acknowledge the U.S. Department of Energy, Energy Efficiency and Renewable Energy, Hydrogen and Fuel Cell Technologies Office (DOE-EERE-HFTO) through the Electrocatalysis Consortium (ElectroCat) and the DOE program managers, Dimitrios Papageorgopoulos and David Peterson. The XAS experiments were performed at the Advanced Photon Source (APS), a DOE Office of Science User Facility operated for the DOE Office of Science by Argonne National Laboratory under Contract No. DE-AC02-06CH11357. The operation of MRCAT at the APS is supported by the Department of Energy and the MRCAT member institutions. The work was performed in part by UChicago Argonne, LLC, Operator of Argonne National Laboratory (“Argonne”), a U.S. Department of Energy Office of Science laboratory under Contract No. DE-AC02-06CH11357. Part of TEM experiments performed at Clemson University Electron Microscopy Facility were supported by Clemson University Startup Fund.

Conflicts of interest

There is no conflict to declare.

References

1. X. X. Wang, M. T. Swihart and G. Wu, *Nature Catalysis*, **2**, 578 (2019).
2. Y. Wang, H. Su, Y. He, L. Li, S. Zhu, H. Shen, P. Xie, X. Fu, G. Zhou, C. Feng, D. Zhao, F. Xiao, X. Zhu, Y. Zeng, M. Shao, S. Chen, G. Wu, J. Zeng and C. Wang, *Chemical Reviews*, **120**, 12217 (2020).
3. Y. Li, H. Wang, C. Priest, S. Li, P. Xu and G. Wu, *Advanced Materials*, **33**, 2000381 (2021).

4. X. X. Wang, V. Prabhakaran, Y. He, Y. Shao and G. Wu, *Advanced Materials*, **31**, 1805126 (2019).
5. Y. Mun, S. Lee, K. Kim, S. Kim, S. Lee, J. W. Han and J. Lee, *Journal of the American Chemical Society*, **141**, 6254 (2019).
6. X. Zhao, X. Yang, M. Wang, S. Hwang, S. Karakalos, M. Chen, Z. Qiao, L. Wang, B. Liu and Q. Ma, *Applied Catalysis B: Environmental*, **279**, 119400 (2020).
7. Y. He, S. Liu, C. Priest, Q. Shi and G. Wu, *Chemical Society Reviews*, **49**, 3484 (2020).
8. Z. W. Seh, J. Kibsgaard, C. F. Dickens, I. Chorkendorff, J. K. Nørskov and T. F. Jaramillo, *Science*, **355**, eaad4998 (2017).
9. Y. Zhu, J. Sokolowski, X. Song, Y. He, Y. Mei and G. Wu, *Advanced Energy Materials*, **10**, 1902844 (2020).
10. Q. Shi, S. Hwang, H. Yang, F. Ismail, D. Su, D. Higgins and G. Wu, *Materials Today*, **37**, 93 (2020).
11. B. Qiao, A. Wang, X. Yang, L. F. Allard, Z. Jiang, Y. Cui, J. Liu, J. Li and T. Zhang, *Nature chemistry*, **3**, 634 (2011).
12. C. Zhu, S. Fu, Q. Shi, D. Du and Y. Lin, *Angewandte Chemie International Edition*, **56**, 13944 (2017).
13. J. Li, M. Chen, D. A. Cullen, S. Hwang, M. Wang, B. Li, K. Liu, S. Karakalos, M. Lucero, H. Zhang, C. Lei, H. Xu, G. E. Sterbinsky, Z. Feng, D. Su, K. L. More, G. Wang, Z. Wang and G. Wu, *Nature Catalysis*, **1**, 935 (2018).
14. X. Xie, C. He, B. Li, Y. He, D. A. Cullen, E. C. Wegener, A. J. Kropf, U. Martinez, Y. Cheng, M. H. Engelhard, M. E. Bowden, M. Song, T. Lemmon, X. S. Li, Z. Nie, J. Liu, D.

J. Myers, P. Zelenay, G. Wang, G. Wu, V. Ramani and Y. Shao, *Nature Catalysis*, **3**, 1044 (2020).

15. N. R. Sahraie, U. I. Kramm, J. Steinberg, Y. Zhang, A. Thomas, T. Reier, J.-P. Paraknowitsch and P. Strasser, *Nature communications*, **6**, 8618 (2015).

16. X. Wang, Y. Jia, X. Mao, D. Liu, W. He, J. Li, J. Liu, X. Yan, J. Chen and L. Song, *Advanced Materials*, 2000966 (2020).

17. M. Xiao, J. Zhu, L. Ma, Z. Jin, J. Ge, X. Deng, Y. Hou, Q. He, J. Li and Q. Jia, *ACS Catalysis*, **8**, 2824 (2018).

18. C. Zhu, S. Fu, J. Song, Q. Shi, D. Su, M. H. Engelhard, X. Li, D. Xiao, D. Li and L. Estevez, *Small*, **13**, 1603407 (2017).

19. Y. Chen, S. Ji, Y. Wang, J. Dong, W. Chen, Z. Li, R. Shen, L. Zheng, Z. Zhuang and D. Wang, *Angewandte Chemie International Edition*, **56**, 6937 (2017).

20. W.-J. Jiang, L. Gu, L. Li, Y. Zhang, X. Zhang, L.-J. Zhang, J.-Q. Wang, J.-S. Hu, Z. Wei and L.-J. Wan, *Journal of the American Chemical Society*, **138**, 3570 (2016).

21. Y. He, Q. Shi, W. Shan, X. Li, A. J. Kropf, E. C. Wegener, J. Wright, S. Karakalos, D. Su, D. A. Cullen, G. Wang, D. J. Myers and G. Wu, *Angewandte Chemie International Edition*, **60**, [10.1002/anie.202017288](https://doi.org/10.1002/anie.202017288) (2021).

22. H. Zhang, H. T. Chung, D. A. Cullen, S. Wagner, U. I. Kramm, K. L. More, P. Zelenay and G. Wu, *Energy & Environmental Science* (2019).

23. H. Shen, E. Gracia-Espino, J. Ma, H. Tang, X. Mamat, T. Wagberg, G. Hu and S. Guo, *Nano Energy*, **35**, 9 (2017).

24. Q. Lai, L. Zheng, Y. Liang, J. He, J. Zhao and J. Chen, *Acs Catalysis*, **7**, 1655 (2017).

25. R. Jiang, L. Li, T. Sheng, G. Hu, Y. Chen and L. Wang, *Journal of the American Chemical Society*, **140**, 11594 (2018).

26. K. S. Park, Z. Ni, A. P. Côté, J. Y. Choi, R. Huang, F. J. Uribe-Romo, H. K. Chae, M. O'Keeffe and O. M. Yaghi, *Proceedings of the National Academy of Sciences*, **103**, 10186 (2006).

27. J. Cravillon, S. Münzer, S.-J. Lohmeier, A. Feldhoff, K. Huber and M. Wiebcke, *Chemistry of Materials*, **21**, 1410 (2009).

28. S. Liu, M. Wang, X. Yang, Q. Shi, Z. Qiao, M. Lucero, Q. Ma, K. L. More, D. A. Cullen, Z. Feng and G. Wu, *Angewandte Chemie International Edition*, **59**, 21698 (2020).

29. D. Crawford, J. Casaban, R. Haydon, N. Giri, T. McNally and S. L. James, *Chemical Science*, **6**, 1645 (2015).

30. Q. Gan, K. Zhao, S. Liu and Z. He, *Electrochimica Acta*, **250**, 292 (2017).

31. Y. Pan, Y. Liu, G. Zeng, L. Zhao and Z. Lai, *Chemical Communications*, **47**, 2071 (2011).

32. M. Chen, Y. He, J. S. Spendelow and G. Wu, *ACS Energy Letters*, **4**, 1619 (2019).

33. M. Newville, *Journal of Synchrotron Radiation*, **8**, 322 (2001).

34. P. Cheng and Y. H. Hu, *The Journal of Physical Chemistry C*, **118**, 21866 (2014).

35. S. Dissegna, K. Epp, W. R. Heinz, G. Kieslich and R. A. Fischer, *Advanced Materials*, **30**, 1704501 (2018).

36. X. Wan, X. Liu, Y. Li, R. Yu, L. Zheng, W. Yan, H. Wang, M. Xu and J. Shui, *Nature Catalysis*, **2**, 259 (2019).

37. M. Chen, X. Li, F. Yang, B. Li, T. Stracensky, S. Karakalos, S. Mukerjee, Q. Jia, D. Su and G. Wang, *ACS Catalysis*, **10**, 10523 (2020).

38. G. Wu, M. Nelson, S. Ma, H. Meng, G. Cui and P. K. Shen, *Carbon*, **49**, 3972 (2011).

39. H. Zhang, S. Hwang, M. Wang, Z. Feng, S. Karakalos, L. Luo, Z. Qiao, X. Xie, C. Wang, D. Su, Y. Shao and G. Wu, *Journal of the American Chemical Society*, **139**, 14143 (2017).

40. J. Li, H. Zhang, W. Samarakoon, W. Shan, D. A. Cullen, S. Karakalos, M. Chen, D. Gu, K. L. More, G. Wang, Z. Feng, Z. Wang and G. Wu, *Angewandte Chemie International Edition*, **58**, 18971 (2019).

41. X. Wang, J. Zhou, H. Fu, W. Li, X. Fan, G. Xin, J. Zheng and X. Li, *Journal of Materials Chemistry A*, **2**, 14064 (2014).

42. Y.-J. Lee, *Journal of nuclear materials*, **325**, 174 (2004).

43. X. Miao, K. Pan, Q. Pan, W. Zhou, L. Wang, Y. Liao, G. Tian and G. Wang, *Electrochimica Acta*, **96**, 155 (2013).

44. H. Liang, B. Song, P. Peng, G. Jiao, X. Yan and D. She, *Chemical Engineering Journal*, **367**, 9 (2019).

45. Z. Qiao, S. Hwang, X. Li, C. Wang, W. Samarakoon, S. Karakalos, D. Li, M. Chen, Y. He, M. Wang, Z. Liu, G. Wang, H. Zhou, Z. Feng, D. Su, J. S. Spendelow and G. Wu, *Energy & Environmental Science*, **12**, 2830 (2019).

46. R. Guo, C. Lv, W. Xu, J. Sun, Y. Zhu, X. Yang, J. Li, J. Sun, L. Zhang and D. Yang, *Advanced Energy Materials*, **10**, 1903652 (2020).

47. A. Reina, X. Jia, J. Ho, D. Nezich, H. Son, V. Bulovic, M. S. Dresselhaus and J. Kong, *Nano letters*, **9**, 30 (2009).

48. Y. He, H. Guo, S. Hwang, X. Yang, Z. He, J. Braaten, S. Karakalos, W. Shan, M. Wang, H. Zhou, Z. Feng, K. L. More, G. Wang, D. Su, D. A. Cullen, L. Fei, S. Litster and G. Wu, *Advanced Materials*, **32**, 2003577 (2020).

49. U. Martinez, S. Komini Babu, E. F. Holby, H. T. Chung, X. Yin and P. Zelenay, *Advanced Materials*, 1806545 (2019).

50. Y. Shao, J. P. Dodelet, G. Wu and P. Zelenay, *Advanced Materials*, 1807615 (2019).

51. U. I. Kramm, M. Lefèvre, P. Bogdanoff, D. Schmeißer and J.-P. Dodelet, *The journal of physical chemistry letters*, **5**, 3750 (2014).

52. L. Osmieri, L. Pezzolato and S. Specchia, *Current Opinion in Electrochemistry*, **9**, 240 (2018).

53. Q. Shi, Y. He, X. Bai, M. Wang, D. A. Cullen, M. Lucero, X. Zhao, K. L. More, H. Zhou, Z. Feng, Y. Liu and G. Wu, *Energy & Environmental Science*, **13**, 3544 (2020).

54. Y. He, S. Hwang, D. A. Cullen, M. A. Uddin, L. Langhorst, B. Li, S. Karakalos, A. J. Kropf, E. C. Wegener, J. Sokolowski, M. Chen, D. Myers, D. Su, K. L. More, G. Wang, S. Litster and G. Wu, *Energy & Environmental Science*, **12**, 250 (2019).

55. C. H. Choi, C. Baldizzone, J. P. Grote, A. K. Schuppert, F. Jaouen and K. J. Mayrhofer, *Angewandte Chemie International Edition*, **54**, 12753 (2015).

56. C. H. Choi, H.-K. Lim, M. W. Chung, G. Chon, N. R. Sahraie, A. Altin, M.-T. Sougrati, L. Stievano, H. S. Oh and E. S. Park, *Energy & environmental science*, **11**, 3176 (2018).

57. R. Chenitz, U. I. Kramm, M. Lefèvre, V. Glibin, G. Zhang, S. Sun and J.-P. Dodelet, *Energy & Environmental Science*, **11**, 365 (2018).

58. G. Zhang, R. Chenitz, M. Lefèvre, S. Sun and J.-P. Dodelet, *Nano Energy*, **29**, 111 (2016).

59. S. Liu, Q. Shi and G. Wu, *Nature Catalysis*, **4**, 6 (2021).